# Simulation of an Isolated Tiltrotor in Hover with an Unstructured Overset-Grid RANS Solver

E. M. Lee-Rausch
Research Engineer
E.Lee-Rausch@nasa.gov

R. T. Biedron
Research Scientist
Robert.T.Biedron@nasa.gov
Computational AeroSciences Branch
NASA Langley Research Center, Hampton, VA 23681

**An unstructured overset-grid Reynolds Averaged Navier-Stokes (RANS) solver, FUN3D, is used to simulate an isolated tiltrotor in hover. An overview of the computational method is presented as well as the details of the overset-grid systems. Steady-state computations within a noninertial reference frame define the performance trends of the rotor across a range of the experimental collective settings. Results are presented to show the effects of off-body grid refinement and blade grid refinement. The computed performance and blade loading trends show good agreement with experimental results and previously published structured overset-grid computations. Off-body flow features indicate a significant improvement in the resolution of the first perpendicular blade vortex interaction with background grid refinement across the collective range. Considering experimental data uncertainty and effects of transition, the prediction of figure of merit on the baseline and refined grid is reasonable at the higher collective range- within 3 percent of the measured values. At the lower collective settings, the computed figure of merit is approximately 6 percent lower than the experimental data. A comparison of steady and unsteady results show that with temporal refinement, the dynamic results closely match the steady-state noninertial results which gives confidence in the accuracy of the dynamic overset-grid approach.**

## Nomenclature

| | |
|---|---|
| $a$ | speed of sound |
| $A$ | rotor disk area, $\pi R^2$ |
| $c$ | local blade chord length |
| $c_{root}$ | root blace chord length |
| $c_{tip}$ | tip blace chord length |
| $C_Q$ | Thrust coefficient, $\frac{Q}{rho(\Omega R)^2 A}$ |
| $C_T$ | Torque coefficient, $\frac{T}{rho(\Omega R)^2 A}$ |
| $FM$ | figure of merit, $\frac{C_T^{3/2}}{C_Q\sqrt{2}}$ |
| $F_n$ | rotor normal force |
| $M$ | Mach number |
| $M_{tip}$ | tip Mach number, $\frac{\Omega R}{a}$ |
| $M^2C_n$ | sectional normal force coefficient, $\frac{F_n}{\frac{1}{2}\rho a^2 c}$ |
| $Q$ | rotor torque |
| $r$ | radial position |
| $R$ | rotor radius |
| $Re$ | Reynolds number |
| $T$ | rotor thrust |
| $\rho$ | air density |
| $\sigma$ | rotor solidity |
| $\Theta$ | blade collective angle at $r/R$=0.75, degrees |
| $\Omega$ | rotor rotational speed, radians/second |

Presented at the American Helicopter Society 65th Annual Forum, Grapevine, TX, May 27-29,2009. 

## Introduction

The development of computational methods for rotorcraft flowfield analysis has lagged behind that of its fixed wing counterpart by as much as a decade according to one estimate.[1] The accurate simulation of a complete rotorcraft flowfield requires modeling the complex interaction of the aerodynamics, structural dynamics and trim. In the engineering design environment, rotorcraft flowfields can be simulated using comprehensive codes in which all facets of the rotorcraft problem are combined using simplified analyses for each facet. According to a recent assessment by the NASA Subsonic Rotary Wing Program, "Though the various comprehensive codes have provided significant benefits for understanding rotorcraft aeromechanics, more detailed analysis and design approaches based on 'first principle methods' are needed to help quantify the complex nonlinear interactions that exist between the various rotorcraft aeromechanics disciplines."[1] As a part of this first principles approach, coupled computational structural dynamics/computational fluid dynamics (CSD/CFD) methods for rotorcraft aeromechanics analysis are currently under development at NASA for the unstructured grid Reynolds Averaged Navier-Stokes (RANS) flow solver, FUN3D, whereby the relative motion of the rotor is modeled by utilizing overset moving grids for the individual blades. The use of unstructured grids is expected to make

the inclusion of rotorcraft fuselages and other components in computational analysis much easier than current structured-grid approaches.[2] The unstructured grid CFD approach also can provide the mechanism for the application of solution adaptive grids.

The FUN3D coupled method has been used to analyze the HART-II wind-tunnel model for three forward flight cases, including effects of the fuselage (fairing/sting).[3] Computed results for both aerodynamic loading and blade structural response were found to be in general good agreement with measured airload and blade deflection data and also with solutions from the state-of-the-art structured grid RANS solver OVERFLOW-2 on computational grids of comparable resolution. The purpose of the current work is to further validate the FUN3D unstructured overset capability for rotor performance in hover. Prediction of rotor performance in hover is a challenging problem due to the persistence of the rotor wake in close proximity to the blade which has a significant effect on the hover figure of merit. The test case chosen for the current work is an isolated tiltrotor wind-tunnel model whose rigid structure allows for CFD analysis uncoupled from structural analysis. Although analysis of an isolated rotor does not exercise the ability of the unstructured grid method to easily handle complex geometry, it is a necessary step for code validation. Analyzing an isolated rotor in hover also allows for comparisons between time-marching and steady-state (noninertial) computations to assess the temporal convergence and accuracy of the dynamic overset grid capability.

Computational fluid dynamics methods for rotorcraft hover analysis have been dominated in recent years by structured-grid finite-volume RANS solvers. The overset-grid RANS solvers OVERFLOW-D and OVERFLOW-2 are quite accurate in predicting the performance of tiltrotors in hover.[4,5] Sliding grid approaches have also been developed in structured grid[6] and unstructured grid[7–9] RANS solvers for rotorcraft analysis. Reference 7 showed good correlation of surface pressures for a two-bladed rotor in hover for a noninertial unstructured grid simulation although in this application without the use of sliding grids. Other finite-volume unstructured grid RANS solvers have implemented an overset grid capability, but none to date have applied the solvers to rotorcraft hover performance analysis. Finite-element approaches using a discontinuous Galerkin (DG) formulation of the Euler equations have been used for hover performance analysis,[10,11] but these analyses have not been applied to the solution of the RANS equations for rotorcraft analysis. The current work represents a first application of the FUN3D unstructured overset-grid solver to the prediction of rotorcraft hover performance.

## Tilt Rotor Aeroacoutics Model (TRAM)

The Tilt Rotor Aeroacoustics Model (TRAM) is a wind tunnel model constructed and tested to facilitate tiltrotor aeromechanics research. This model provides a significant source of aeroacoustic, performance, and structural loads data for validation of tiltrotor analyses. The geometry is a 0.25-scale V-22 nacelle and 3-bladed rotor with geometric and dynamic scaling. The airfoil sections of the TRAM rotor are similar to the V-22 except those sections at the blade root fairing which have been modified. The V-22 rotor blade has a large amount of nonlinear twist as well as thick inboard airfoil sections which is typical of tiltrotors but significantly different from conventional helicopter rotor configurations. The centerbody is a V-22 spinner with a faired boattail. Due to the rigid nature of the wind tunnel model structure, it was not necessary to model the elastic blade effects in the computational analysis. Details of the model and geometry have been described in Ref. 12.

The isolated TRAM rotor was tested in the Duits-Nederlandse Windtunnel Large Low-speed Facility (DNW-LLF). A photo of the model in the facility is shown in Fig. 1. Details of the test and data reduction are described in Refs. 13 and 14. Hover runs were performed at nominal tip Mach numbers of 0.58 and 0.62, rather than the V-22 hover tip Mach number of 0.72 due to rotor operational limitations. The tip chord Reynolds number was 2.1 million. The rotor collective setting was varied over a range of $\Theta = 3 - 17°$. Hover testing was performed in both helicopter mode (shown in Fig. 1) and airplane mode. According to Johnson,[12] performance data for the airplane mode is more accurate due a reduction of support blockage and interference. Therefore, the experimental performance data for the airplane mode will be used for comparison with computations in this study. The TRAM geometric characteristics and nominal test parameters in hover are summarized in Table 1.

| | |
|---|---|
| rotor radius, $R$ | 57 in. |
| solidity, $\sigma$ | 0.105 |
| tip chord, $c_{tip}$ | 5.5 in. |
| twist | 32 to -6°, nonlinear |
| tip Mach number | 0.58, 0.62 |
| tip Re | $2.1 \times 10^6$ |
| $C_T/\sigma$ range | 0.05–0.17 |
| collective range, $\Theta$ | 3–17° |

**Table 1 Summary of TRAM geometric characteristics and nominal test parameters in hover.**

## Computational Method

FUN3D[15–17] is a finite-volume RANS solver in which the flow variables are stored at the vertices of the mesh.

FUN3D solves the equations on mixed element grids, including tetrahedra, pyramids, prisms, and hexahedra. It employs an implicit upwind algorithm in which the inviscid fluxes are obtained with a flux-splitting scheme. At interfaces delimiting neighboring control volumes, the inviscid fluxes are computed using an approximate Riemann solver based on the values on either side of the interface. For second-order accuracy, interface values are obtained by extrapolation of the control volume centroidal values, based on gradients computed at the mesh vertices using an unweighted least-squares technique. Limiting of the reconstructed values may be employed for flows with strong shocks. For tetrahedral meshes, the full viscous fluxes are discretized using a finite-volume formulation in which the required velocity gradients on the dual faces are computed using the Green-Gauss theorem. (On tetrahedral meshes this is equivalent to a Galerkin-type approximation.) For all results presented in this paper, the convective flux scheme used is Roe's flux-difference splitting[18] with no limiting applied.

For steady-state flows, local time-step scaling is employed to accelerate convergence. To advance the equations in time for unsteady flows, several schemes based on backward differentiation formulae (BDF) are available.[19] At each time step, the linear system of equations is approximately solved with either a multi-color point-implicit procedure or an multi-color implicit-line relaxation scheme.[20] For the current work, a second-order scheme is used for time-accurate computations in conjunction with the temporal-error controller described in Ref. 19 that eliminates some of the guesswork involved in determining the proper number of nonlinear subiterations required within a given time step. The mesh motion capabilities in the FUN3D unstructured-mesh, Navier-Stokes flow solver allow for a broad range of moving-geometry applications. The solver has been extended to handle general mesh movement involving rigid, deforming, and overset meshes.[21] A general method for specifying the motion of moving bodies within the mesh has been implemented that allows for inherited motion through parent-child relationships, enabling simulations involving multiple moving bodies. For problems like the current study in which an isolated body is rotating with a fixed rate, a noninertial reference-frame formulation is available. If the problem is steady in the noninertial frame, then a significant reduction in computation time can be achieved over the time required to solve the problem in the inertial frame, where a time-dependent problem must be solved. Moving mesh computations utilize the Geometric Conservation Law[22] to ensure that the scheme is free-stream preserving with moving meshes.

FUN3D is able to solve the RANS flow equations, either tightly or loosely coupled to the Spalart-Allmaras[23] (S-A) one-equation turbulence model. The Menter SST Model[24] is also available for loosely coupled solutions. In all cases presented here, the S-A turbulence model was employed with a Dacles-Mariani correction[25] applied to limit the excessive production of turbulent eddy viscosity in the rotor tip vortices. Note that the turbulence model is solved throughout the entire flowfield. Additionally, all computations are solved with a loose coupling between the turbulence model and mean-flow equations and with an assumption of fully turbulent flow.

The blade surface boundary condition is the standard no-slip viscous boundary. A source-sink model has been advocated in the past for hover computations, but Ref. 4 reported negligible differences between solutions using the source-sink and freestream characteristic boundary condition when the outer boundaries are at least five rotor radius ($5R$) away. For the current application, the grid outer boundaries are 5R away and so the freestream characteristic boundary condition ($M_\infty = 0.0$) is applied.

The overset method was first implemented in the FUN3D solver by O'Brien.[26] The implementation uses the Donor interpolation/Receptor Transaction library[27] (DiRTlib) to facilitate the use of overset grids in a parallel environment without extensive modification to the flow solver. As for non-overset meshes, the flow solver continues to operate on a single mesh (partitioned for multiple processors). For overset meshes, points are flagged with an identifier for the particular component mesh with which they are associated. With a few simple calls within the flow solver, DiRTlib handles the equation blanking and solution interpolation required for the overset method. Linear interpolation of the solution between points associated with different component meshes is used with two layers of donor points, consistent with the underlying second-order spatial accuracy of the baseline solver. Points within holes (blanked regions) are assigned solution values by averaging the solution at neighboring points. This also helps ensure that for moving mesh problems, points that were blanked at previous time steps do not suddenly become unblanked with initial freestream values. Orphan points (if any) are assigned solution values in the same manner as hole points.

DiRTlib does not perform composite grid assembly, cut holes (establish blanking), or determine the requisite interpolation coefficients. For that, the Structured, Unstructured, and Generalized overset Grid AssembleR[28] (SUGGAR) program is employed. SUGGAR may be compiled as a stand-alone executable or as a callable library. In a preprocessing step prior to the initial flow-solver execution, SUGGAR reads two or more component meshes and creates a single composite mesh with the configuration in the initial position, along with a domain connectivity file (a DCI file in SUGGAR/DiRTlib parlance) identifying points corresponding to each component mesh, blanked points, and interpolation coef-

ficients. This composite mesh is then partitioned for execution on multiple processors, after which the flow-solver execution may begin.

## Computational Grids

The baseline composite-grid systems for the TRAM were developed by over-setting component grids for each individual TRAM blade with an empty (background) square domain. Different collective settings are modeled by rotating the individual blade volume grids along the blade pitch axis and creating a new composite grid. The component unstructured grids for the overset computations were generated with VGrid 4.0[29] and are fully tetrahedral grids. The near-body blade grids extended approximately one tip chord ($c_{tip}$) away from the blade to a rectangular outer boundary. In the wall normal direction, the grid spacing is set such that an average normalized coordinate $y^+$ is less than one for the first grid cell at the wall for the majority of the blade. The maximum spacing at the blade grid outer boundary is approximately $0.10c_{tip}$. The characteristic spacings of the baseline rotor grid are summarized in Table 2. Note that these are the spacing values associated with the VGrid "sources" which are used to control the unstructured grid spacing field. The maximum spanwise stretching is 30:1 near the blade leading edge (LE) and 20:1 near the trailing edge (TE). Each component blade grid has approximately 3.5 million nodes.

| | Direction | Characteristic Spacing |
|---|---|---|
| Rotor Surface | chordwise | $0.0056c_{root}$–$0.0012c_{tip}$ LE |
| | | $0.0005c_{root}$–$0.0008c_{tip}$ TE |
| | spanwise | 0.0018R Root |
| | | 0.0060R Mid-Span |
| | | 0.0007R Tip |
| | normal | $0.91 \times 10^{-6} c_{tip}$ |
| | | (geometric stretching 1.18) |
| Rotor Outer Boundary | isotropic | $0.10c_{tip}$ |

**Table 2 Characteristic spacings of baseline rotor grid.**

A spinner grid was created to optionally add to the baseline composite system to investigate its effect on recirculation near the blade root. However, as discussed in the next section, most computations did not include the spinner. The spinner moves with the same rotation rate as the blades, but it is physically separated from the blade. (The connections from the blade to the spinner are not modeled.) The solid surface of the spinner is modeled as inviscid, and the surface discretization is relatively coarse. The spinner component grid has only about 215,000 nodes. The surface grid resolution for the the rotor and spinner baseline component grids is shown in Fig. 2. The blade and spinner surface definitions were provided by Potsdam.[4]

The off-body or background grid is defined in a square box whose sides extends 5R out from the rotor hub. The finest spacing in the off-body grid is approximately $0.10c_{tip}$. This minimum spacing is maintained, within the constraints of the unstructured meshing software, in a cylindrical volume which extends $1.21R$ in the blade plane and $0.24R$ above and $0.58R$ below the blade plane. This cylindrical volume of refinement was achieved by utilizing a new feature of VGrid, volume sources.[30] The background component grid has approximately 4.5 million nodes. The baseline composite grid has a total of approximately 15 million nodes. A slice through the baseline TRAM composite grid in Fig. 3 shows the spacing characteristics of the blade and off-body grids through the computational domain. The grids are shown in a vertical plane passing through a blade quarter-chord. Note that the fringe and hole points are not plotted.

Although a mathematically consistent grid refinement study in the sense of Ref. 31 was not performed, several alternative composite-grid systems were developed to look at the effects of grid refinement: a globally coarsened grid, a refined rotor-grid, and a refined off-body grid. A comparison of global characteristics for these composite grids is provided in Table 3. The coarse composite grid was developed from the baseline grid by increasing the minimum off-body mesh spacing to $0.15c_{tip}$ and reducing the vertical extent of the cylindrical refinement below the rotor plane. The baseline blade grid spacings were also globally coarsened by a factor of 1.7 except for the wall spacing. This coarse composite grid has approximately 5 million nodes. A slice through the coarse TRAM composite grid is compared to the baseline in Fig. 3. A refined rotor grid was developed by globally refining the rotor surface-grid spacings by a factor 0.80. The maximum spacing at the blade grid outer boundary was set to $0.10c_{tip}$ so that this grid could be overset with the baseline off-body grid. The total number of nodes for this refined rotor grid system is approximately 18.1 million. A refined off-body mesh system was developed by adding a toroidal ring of $0.05c_{tip}$ spatial refinement within the baseline grid's region of cylindrical refinement. This torus extends from approximately $0.75R$ to $1.10R$ in the radial direction at $0.04R$ above the blade plane to $0.61R$ to $1.00R$ in the radial direction at $0.44R$ below the blade plane. A similar region of refinement was added to the baseline rotor grid so that the off-body and rotor grids would have consistent spacings in the overset regions. A slice through the refined off-body composite grid in Fig. 3 illustrates the location of the torus (darkest blue region). This composite grid system has approximately 23.1 million nodes.

For all composite grid systems, a stand-alone SUG-

| | | Baseline | Coarse | Refined Blade | Refined Background |
|---|---|---|---|---|---|
| Blade Grid | Nodes (millions) | 3.51 | 1.54 | 4.55 | 3.74 |
| | Viscous Surface Nodes (thousands) | 66 | 31 | 86 | 66 |
| | Characteristic Surface Spacing | 1 | 1.7* | 0.8 | 1 |
| | Characteristic Outer Boundary Spacing | $0.10c_{tip}$ | $0.15c_{tip}$ | $0.10c_{tip}$ | $0.05$–$0.10c_{tip}$ |
| Background Grid | Nodes (millions) | 4.50 | 1.05 | 4.50 | 11.9 |
| | Finest Spacing | $0.10c_{tip}$ | $0.15c_{tip}$ | $0.10c_{tip}$ | $0.05c_{tip}$ |
| | Outer Boundary Extent | 5R | 5R | 5R | 5R |
| Composite Grid | Total Nodes (millions) | 15.0 | 5.67 | 18.15 | 23.1 |

*(except normal direction which is 1)

**Table 3 Comparison of composite grid systems.**

GAR executable was used in a pre-processing step to create the composite grid and the domain connectivity file (DCI) for the initial rotor position. For noninertial cases, these are the only files required. For dynamic overset cases, a DCI file must be created for each azimuthal location which can be done a priori for rigid blade cases. The octree based hole-cutting algorithm was used to define the blanked points in the composite grid, and an overlap minimization process was used to identify fringe points. A donor quality value of 1.0 was specified, and no orphans were generated in the overlap process. The high-quality donor interpolation is achieved by matching the blade-grid outer boundary spacings to the spacing in the background grid. This would be difficult to do without the VGrid volume sources.

## Computational Results

#### Effects of Spinner on Rotor Performance

Computations were initially performed on the baseline grids with and without the spinner at selected collective angles to assess the effects of the spinner on rotor performance. Steady-state noninertial computations were made at a tip Mach number of $0.62$ for two collective settings, $\Theta = 8^\circ$ and $14^\circ$. The inclusion of the spinner geometry had no significant effect on rotor performance at either collective setting for the geometry as modeled. The values of rotor thrust, torque and figure of merit with and without the spinner were the same to within plotting accuracy (third significant figure). Due to the limited effect of the spinner geometry on rotor performance, all subsequent computations for this study have been made without the inclusion of the spinner geometry. A discussion of the spinner effect on the blade-root vortex strength in a subsequent section will highlight that the inclusion of the current spinner geometry has little effect on the flowfield characteristics. It is possible that a more extensive modeling of the rotor blade connections, boattail fairing and support structure might have a significant effect on the computational results. However, these modeling effects have not been considered in this work. No published work to date has included these additional geometric components.

#### Rotor Performance

Computations have been made to define the performance trends of the rotor across the upper end of the experimental collective range. For the coarse (5M nodes) and baseline (15M nodes) composite grids, computations have been performed at a tip Mach number of $0.62$ for five collective settings; $\Theta = 8^\circ$, $10^\circ$, $12^\circ$, $14^\circ$ and $16^\circ$. For the refined-background (23M nodes) grid, computations have been performed for three collective settings; $\Theta = 8^\circ$, $14^\circ$ and $16^\circ$. All of the computations have been made in the noninertial reference frame. For the coarse and baseline grids, local time-step scaling is used to accelerate the residual convergence of the non-linear equations and achieve steady-state values of forces and moments. For the refined-background grids, local time-step scaling fails to achieve a sufficient level of non-linear residual convergence with the forces/ moments remaining oscialltory. However, convergence of the equations on these grids was achieved by switching to a global time-step solution procedure. A similar improvement in steady-state convergence of TRAM forces/moments has been noted in Ref. 4 by turning off local time-stepping.

Comparisons of the computed results with the TRAM DNW hover performance data (airplane mode) are shown in Figs. 4, 5, and 6 including thrust coefficient ($C_T$), torque coefficient ($C_Q$) and figure of merit ($FM$). Overall, the slope of the computed thrust versus collective curve is high compared to the experimental data, and there is a consistent over-prediction of the torque and under-prediction of $FM$ in the computational results at a given thrust level. Looking specifically at the effect of the global grid refinement between the coarse and baseline grid results in Figs. 4-6, the correlation of $C_Q$ and $FM$ with the experimental data is much improved across the collective range with grid refinement while the $C_T$ correlation is improved at the lower collective values but tends to be over-predicted at the upper values.

Computations on the refined-blade grid at $\Theta = 8^\circ$ and $14^\circ$ indicate less sensitivity of the performance trends to the refinement of the blade surface resolution giving a small increase of $0.007$ and $0.002$ in $FM$, respectively, as shown in Fig. 6. (Values of $C_T$ and $C_Q$ from the refined-blade grid computation are the same as the baseline grid values to within plotting accuracy in Figs. 4 and 5, and therefore, they are omitted to maintain clarity.) This lack of sensitivity would imply that the baseline blade grid resolution is sufficient at the higher collective range but should be refined for the lower values of collective. The effects of refining the background grid in the rotor tip-vortex region is not consistent with the effects of the global refinement. Although the $C_T$ increases slightly with the background grid refinement, the $FM$ at the $\Theta = 14^\circ$ and $16^\circ$ collective settings drops slightly with refinement due in part to the more rapid increase in $C_Q$. The $C_T$, $C_Q$ and $FM$ at the $\Theta = 8^\circ$ are relatively insensitive to the background grid refinement. Blade loading and off-body flowfield results shown in subsequent sections of the paper will give insight in the physical causes of these trends.

Steady results from OVERFLOW-2[5] using fourth-order spacial differencing and the S-A turbulence model on a similarly-sized mesh are included in Figs. 4–6 for comparison. The OVERFLOW-2 computations at a $\Theta = 14^\circ$ collective predict a lower thrust than the FUN3D results at the same collective. However, the torque is also lower which results in a similar prediction of $FM$. Ref. 4 reports a probability of laminar flow on the TRAM airfoil and estimates that the fully turbulent computational results may under-predict the experimental $FM$ by as much as 0.014 at $\Theta = 14^\circ$ with part of the effect coming from a decrease in the viscous component of the torque coefficient. Estimates were not made in Ref. 4 at other collective angles. However, noting that the viscous component of torque is approximately 6% of the the total torque at $\Theta = 14^\circ$ and 14% at $\Theta = 8^\circ$, it might be expected that the effects of the fully turbulent assumption on performance may be more significant at the lower collective angles. Therefore for tiltrotor applications, it may be necessary to include some sort of transition estimate or modeling to acheive a higher level of accuracy in performance predictions across the collective range. Considering the experimental data uncertainty and the effects of transition, the prediction of $FM$ is reasonable at the higher collective range – within 3 percent of the measured values. At the lower collective settings, the computed $FM$ is approximately 5-6 percent lower than the experimental data.

**Dynamic Overset Grid**

At $\Theta = 14^\circ$, both time-marching and steady-state noninertial analyses have been made on the baseline grid. The results from the steady-state noninertial case can be thought of as the limiting values for temporal refinement. For the time-marching cases, the blades are moved dynamically through the stationary off-body mesh which is the approach that is required when studying rotor/fuselage interactions. Second-order time-accurate computations have been performed at time-steps corresponding to $1^\circ$ and $0.5^\circ$ increments in azimuth for up to 8-9 rotor revolutions. Performance results for the time-marching cases are included in Fig. 7 along with the noninertial results for the baseline composite grids. With time-step refinement, the correlation of the dynamic unsteady results and the steady noninertial results is much improved. At the refined time step ($0.5^\circ$), the dynamic results closely match the steady-state noninertial results which gives confidence in the accuracy of the dynamic overset grid approach. Steady and unsteady results from OVERFLOW-2[5] at the $\Theta = 14^\circ$ collective setting are also included in Fig. 7 for reference. (The cause of the differences between the noninertial and unsteady results for the OVERFLOW-2 computations are not currently known.[5])

**Blade Loading**

Blade pressures for the TRAM test were measured at seven radial stations during hover testing and integrated to obtain section normal force. (The blade pressures were obtained during testing in the helicopter mode which is thought to have more support blockage and interference than the airplane mode.[12]) Computed normal force distributions from the baseline grids are compared with the experimental values in Fig. 8. The results are shown in terms of blade section normal force coefficient times Mach number squared ($M^2 c_n$) versus normalized blade span location ($r/R$). The trends in spanwise loading and collective are well captured. The over-prediction of the normal force load at the mid-span and tip at the higher collective settings is consistent with previously published OVERFLOW-D results.[4] (The OVERFLOW-D results also did not show the dip in normal force at the $r/R = 0.70$ span location as indicated by the experimental results.)

The effects of grid refinement on sectional normal force are shown in Fig. 9 for the $\Theta = 8^\circ$, $14^\circ$ and $16^\circ$ collective settings. At $\Theta = 8^\circ$, the loading from 20% to 80% span is hardly affected while the peak tip loading is increasing monotonically with grid refinement. For the refined-background grid, the peak is not as broad resulting in a small loss of loading around 80% span. These trends help explain the effects of grid refinement on the $C_T$ shown in the previous section. (Note that the peak in sectional normal force near the tip is due in part to the passage of the preceding blade's tip vortex near the tip.) At $\Theta = 14^\circ$ and $16^\circ$, a slight loading increase is

observed from 20% to 80% span as the grids are refined. The tip loading increases monotonically with coarse to baseline grid refinement but then drops back to the coarse grid levels for the refined-background grid solutions and shift slightly inboard. These trends also help explain the effects of grid refinement on the $C_T$ shown in the previous section, but leave the question as to why the peak values of loading drop with background grid refinement. A similar trend in sectional normal force distributions with background grid refinement was noted in Ref. 4 for OVERFLOW-D computations at $\Theta = 14°$. The changes in tip loading are due to the variations in the strength and location of the preceding blades' tip vortices with grid refinement. These flowfield characteristics will be further discussed in the next section.

A small area of flow separation is found on the inboard portion of the blade at all collective angles. A comparison of surface-restricted streamlines in the blade reference frame is shown in Fig. 10 for four composite grid resolutions at the $\Theta = 14°$ collective angle: coarse, baseline, refined background and refined rotor. The surface streamlines for all grid resolutions indicate a mild flow separation on the cuff and inboard part of the blade. The separated flow area on the coarse grid is somewhat larger than on the baseline grid, but the streamlines on the baseline, refined-background and refined-rotor grids are very similar. This pattern of flow separation is consistent with the previously reported OVERFLOW-D results.[4] Reference 4 also noted that the areas of observed flow reversal in the computations qualitatively match skin friction measurements on a full-scale XV-15 at similar collective angles and loading conditions.

#### Off-Body Flowfield Characteristics

Off-body flow features discussed in the next section will illustrate the effects of the grid refinement and collective angle on the vortical structure of the flowfield. The effects of grid refinement on vorticity magnitude are shown on Figs. 11, 12, and 13 for the $\Theta = 8°$, $14°$ and $16°$ collective settings, respectively. Vorticity magnitude contour lines are shown in a vertical plane passing through a blade quarter-chord. The range of contour values is $0.0 - 0.026$ in increments of $0.002$. The view is from the trailing edge of the blade such that the tip vortices in proximity to the blade surface shown on the right side of the figures have wake ages of $120°$, $240°$ and $360°$. The vortices on the left have wake ages of $60°$, $180°$ and $240°$. The cylindrical refinement volume in the baseline grid encompasses the entire plotting area shown in Figs. 11–13. The cylindrical refinement volume in the coarse grid encompasses only the top half of the plotting area. The extent of the toroidal ring of refinement in the refined-background grid is outlined in Figs. 11–13 to illustrate the vortex positions in relation to the grid refinement.

At $\Theta = 8°$, the vortex associated with the first perpendicular blade-vortex interaction (BVI) is quite diffuse and has a small peak magnitude on the coarse and baseline grids. However in the refined-background grid solution, the first BVI vortex core has a much smaller radius and higher peak vorticity. The trailing vortices with larger wake ages do not show as significant an effect with grid refinement and are still diffused. Further a priori refinement in the tip vortex region would be possible with the current computational approach. However in the long term, a more practical approach to capturing the weaker vortex structures may require the use of adaptive grid refinement and/or higher order spatial methods. At $\Theta = 14°$ and $16°$, a similar trend with grid refinement is shown for the vortex associated with the first BVI. However unlike the $\Theta = 8°$ grid refinement trends, at the higher collective angles the trailing vortices with larger wake ages show a more significant effect due to grid refinement especially at the $240°$ and $180°$ wake ages. The influence of these stronger and more compact vortices is to move the location of the first BVI vortex core further below the blade. (This movement of the vortex would be consistent with the reduction in sectional normal force for $\Theta = 14°$ and $16°$ results on the refined-background grid.) Figures 12 and 13 show that the vortices at $240°$ and $360°$ wake ages (the bottom vortices on the left and right sides) start to convect out of the refined-background areas. Refinement of the grid further below the plane of the rotor could have an influence on the strength and vertical spacing of the trailing vortices which could in turn affect rotor performance values.

At all collective angles and grid resolutions, the blade root vortices are quite strong although they do not persist as long as the tip vortices. A comparison of vorticity magnitude contours for $\Theta = 14°$ with and without the spinner shown in Fig. 14 also indicates that the blade-root vortices are still quite strong even with the spinner in place. It is possible that the blade-root vortices may be over-predicted in the current computation due to the sheared-off modeling of the blade root. However, the effect of these vortices on the rotor performance is uncertain.

## Summary

An unstructured overset-grid RANS solver, FUN3D, has been used to simulate an isolated tiltrotor in hover. An overview of the computational method has been presented as well as the details of the grids used for the computations. Initial computations indicated that the spinner geometry as modeled here without connecting hardware did not have a significant effect on the performance values of the rotor and so this component was not included in the majority of the computations. Steady-

state noninertial computations have been made to define the performance trends of the rotor across the upper end of the experimental collective range. Results on coarsened and refined grids have been presented to show the effects of global, off-body grid and blade grid refinement. The computed performance trends and blade loading trends generally showed good agreement with experimental results and previously published OVERFLOW-D and OVERFLOW-2 computations. The grid-refinement trends also showed good agreement with the previously published OVERFLOW-D computations. Considering experimental data uncertainty and effects of transition, the prediction of $FM$ on the baseline and refined grid is reasonable at the higher collective range – within 3 percent of the measured values. At the lower collective settings, the computed figure of merit is approximately 6 percent lower than the experimental data.

A comparison of steady and unsteady results show that with temporal refinement, the dynamic results closely match the steady-state noninertial results which gives confidence in the accuracy of the dynamic overset-grid approach. Off-body flow features presented indicated a significant improvement in the resolution of the first BVI vortex core with background grid refinement across the collective range. The resolution of the trailing vortices at larger wake ages were also improved with grid refinement at the higher collective settings resulting in a drop the vertical position of the first BVI vortex core further below the blade. However at a lower collective setting, the trailing vortices with larger wake ages did not show as significant of an effect with grid refinement and were still diffused. It is unclear from the current computations whether further grid refinement would significantly strengthen the tailing vortices and subsequently influence rotor performance predictions. At all collective angles and grid resolutions, the predicted blade-root vortices are quite strong and are not influenced by the presence of the spinner.

## Acknowledgments

The authors would like to thank Drs. Mark Potsdam and Roger Strawn, Aeroflightdynamics Directorate (AMRDEC), for providing the TRAM blade and spinner surface definitions and also for the insightful discussions on hover boundary conditions and OVERFLOW TRAM computations. The authors would also like to thank Dr. Ralph Noack, The Pennsylvania State University, for the many helpful discussions on the use of SUGGAR and DiRTlib.

## References

[1]Yamauchi, G. K. and Young, L. A., editors, *A Status of NASA Rotorcraft Research*, NASA/TP-2009-215369, 2009.

[2]Sitaraman, J., Katz, A., Jayaraman, B., Wissink, A. M., and Sankaran, V., "Evaluation of a Multi-Solver Paradigm for CFD using Overset Unstructured and Structured Adaptive Cartesian Grids," AIAA Paper 2008-660, Jan. 2008.

[3]Biedron, R. T. and Lee-Rausch, E. M., "Rotor Airloads Prediction Using Unstructured Meshes and Loose CFD/CSD Coupling," AIAA Paper 2008-7341, Aug. 2008.

[4]Potsdam, M. A. and Strawn, R. C., "CFD Simulation of Tiltrotor Configuration in Hover," *American Helicopter Society 58$^{th}$ Annual Forum Proceedings*, 2002.

[5]Potsdam, M. A. and Pulliam, T., "Turbulence Modeling Treatment for Rotorcraft Wakes," *American Helicopter Society Specialist's Conference on Aeromechanics*, 2008.

[6]Steijl, R. and Barakos, G., "Computational Analysis of Rotor-Fuselage Interactional Aerodynamics Using Sliding-Plane CFD Method," *34$^{th}$ European Rotorcraft Forum, Liverpool, UK*, 2008.

[7]Sheng, C. and Wang, X., "Characteristic Variable Boundary Conditions for Arbitrary Mach Number Algorithm in Rotating Frame," AIAA Paper 2003-3976, June 2003.

[8]Sheng, C. and Narramore, J. C., "Unsteady Simulations of Bell-Agusta 609 Rotor Undergoing Higher Harmonic Oscillation," *Journal of Aircraft*, Vol. 45, No. 3, May 2008, pp. 971–980.

[9]Nam, H. J., Park, Y., and Kwon, O. J., "Simulation of Unsteady Rotor-Fuselage Aerodynamic Interaction Using Unstructured Adaptive Meshes," *Journal of the American Helicopter Society*, Vol. 51, No. 2, 2006, pp. 141–148.

[10]Modisette, J. M. and Darmofal, D. L., "An Output-based Adaptive and Higher-Order Method for a Rotor in Hover," AIAA Paper 2008-7343, Aug. 2008.

[11]Boelens, O. J., van der Ven, H., Kok, J. C., and Prananta, B. B., "Rotorcraft Simulations Using Sliding-Grid Approach," *34$^{th}$ European Rotorcraft Forum, Liverpool, UK*, 2008.

[12]Johnson, W., "Calculation of Tilt Rotor Aeroacoutic Model (TRAM DNW) Performance, Airloads, and Structural Loads," *American Helicopter Society Aeromechanics Specialists' Meeting*, 2000.

[13]Young, L. A., Booth Jr., E. R., Yamauchi, G. K., Botha, G., and Dawson, S., "Overview of the Testing of a Small-Scale Proprotor," *American Helicopter Society 55$^{th}$ Annual Forum Proceedings*, 1999.

[14]Swanson, S. M., McCluer, M. S., Yamauchi, G. K., and Swanson, A. A., "Airloads Measurements from a 1/4-Scale Tiltrotor Wind Tunnel Test," *25$^{th}$ European Rotorcraft Forum, Rome, Italy*, 1999.

[15]Anderson, W. K. and Bonhaus, D. L., "An Implicit

Upwind Algorithm for Computing Turbulent Flows on Unstructured Grids," *Computers and Fluids*, Vol. 23, No. 1, 1994, pp. 1–22.

[16]Anderson, W. K., Rausch, R. D., and Bonhaus, D. L., "Implicit/Multigrid Algorithms for Incompressible Turbulent Flows on Unstructured Grids," *Journal of Computational Physics*, Vol. 128, No. 2, 1996, pp. 391–408.

[17]Nielsen, E. J., *Aerodynamic Design Sensitivities on an Unstructured Mesh Using the Navier-Stokes Equations and a Discrete Adjoint Formulation*, Ph.D. thesis, Virginia Polytechnic Institute and State University, Blacksburg, VA, 1998.

[18]Roe, P. L., "Approximate Riemann Solvers, Parameter Vectors, and Difference Schemes," *Journal of Computational Physics*, Vol. 43, 1981, pp. 357–372.

[19]Biedron, R. T., Vatsa, V. N., and Atkins, H. L., "Simulations of Unsteady Flows Using an Unstructured Navier-Stokes Solver on Moving and Stationary Grids," AIAA Paper 2005-5093, June 2005.

[20]Nielsen, E. J., Lu, J., Park, M. A., and Darmofal, D. L., "An Implicit, Exact Dual Adjoint Solution Method Implicit, Exact Dual Adjoint Solution Method for Turbulent Flows on Unstructured Grids," *Computers and Fluids*, Vol. 33, No. 9, 2004, pp. 1131–1155, See also AIAA Paper 2003–0272.

[21]Biedron, R. T. and Thomas, J. T., "Recent Enhancements to the FUN3D Flow Solver for Moving Mesh Applications," AIAA Paper 2009-1360, Jan. 2009.

[22]Thomas, P. D. and Lombard, D. K., "Geometrical Conservation Law and Its Application," *AIAA Journal*, Vol. 17, No. 10, Oct. 1978, pp. 1030–1037.

[23]Spalart, P. R. and Allmaras, S. R., "One-Equation Turbulence Model for Aerodynamic Flows," AIAA Paper 92–0429, 1992.

[24]Menter, F. R., "Two-Equation Eddy-Viscosity Turbulence Models for Engineering Applications," *AIAA Journal*, Vol. 32, No. 8, 1994, pp. 1598–1605.

[25]Dacles-Mariani, J., Zilliac, G. G., Chow, J. S., and Bradshaw, P., "Numerical/Experimental Study of a Wingtip Vortex in Near Field," *AIAA Journal*, Vol. 33, No. 9, 1995, pp. 1561–1568.

[26]O'Brien, D., *Analysis of Computational Modeling Techniques for Complete Rotorcraft Configurations*, Ph.D. thesis, Georgia Institute of Technology, 2006.

[27]Noack, R. W., "DiRTlib: A Library to Add an Overset Capability to Your Flow Solver," AIAA Paper 2005-5116, June 2005.

[28]Noack, R. W., "SUGGAR: a General Capability for Moving Body Overset Grid Assembly," AIAA Paper 2005-5117, June 2005.

[29]Pirzadeh, S., "Three-Dimensional Unstructured Viscous Grids by the Advancing Front Method," *AIAA Journal*, Vol. 34, No. 1, Jan. 1996, pp. 43–49.

[30]Pirzadeh, S. Z., "Advanced Unstructured Grid Generation for Complex Aerodynamic Application," AIAA Paper 2008-7178, Aug. 2008.

[31]Thomas, J. L., Diskin, B., and Rumsey, C. L., "Towards Verification of Unstructured-Grid Solvers," AIAA Paper 2008-0666, Jan. 2008.

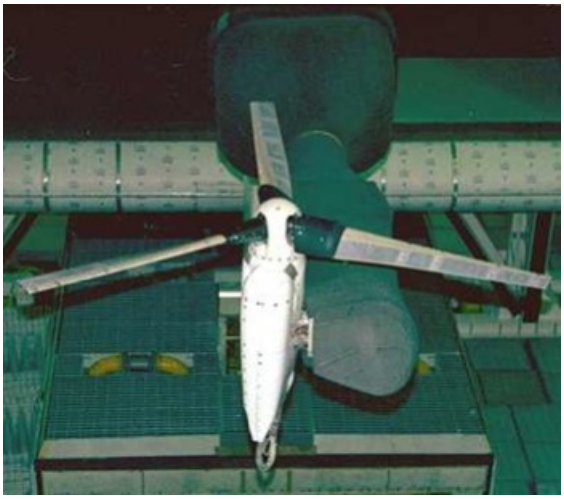

(a) Helicopter mode

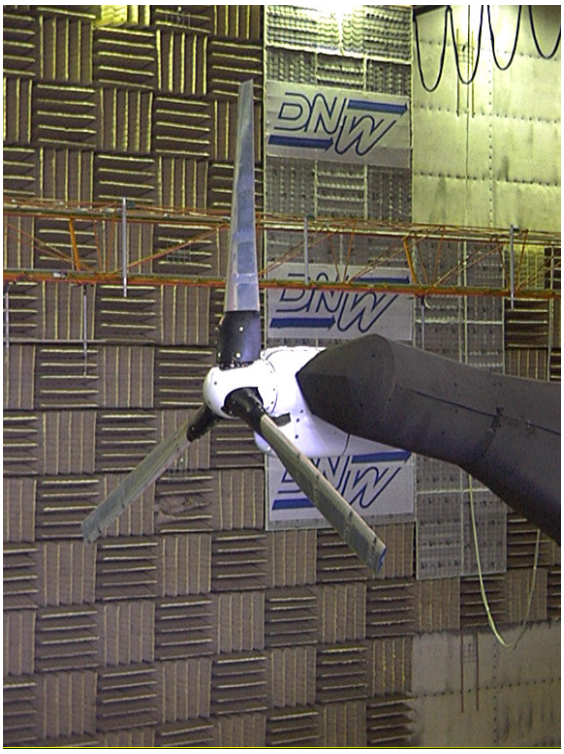


(b) Airplane mode

**Fig. 1 Tilt Rotor Aeroacoutics Model (TRAM) in DNW wind tunnel.**

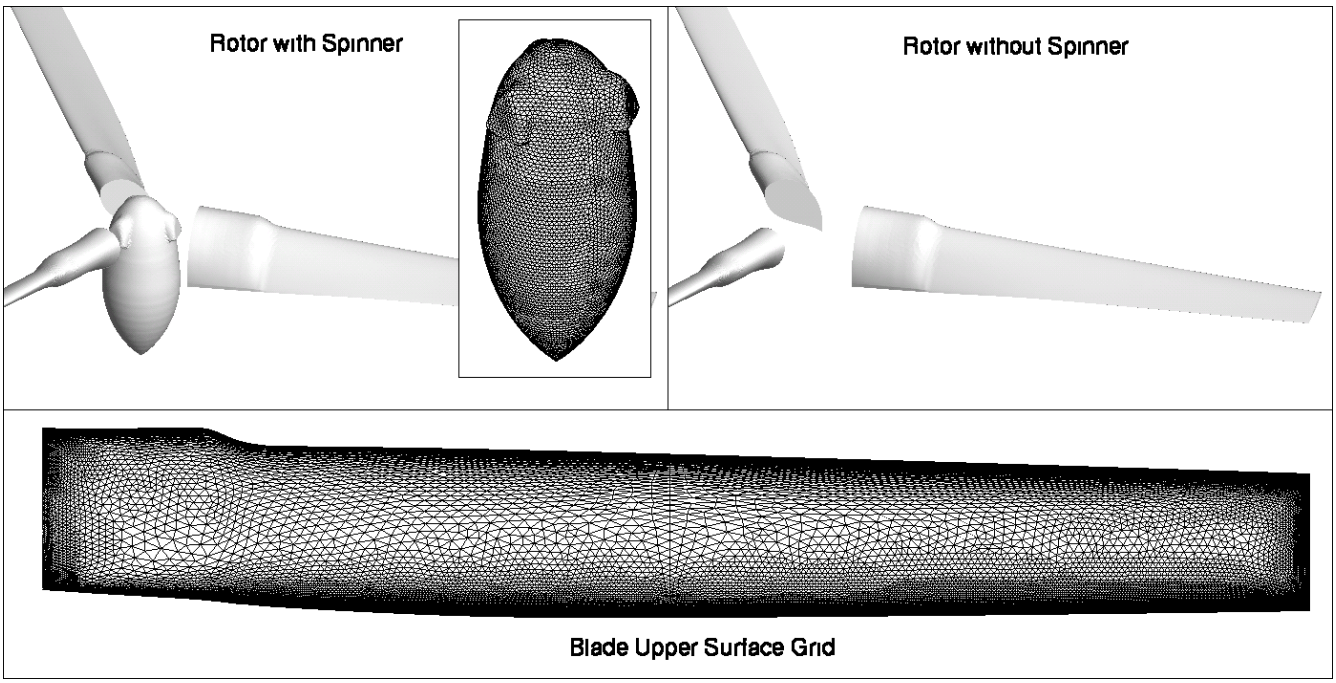


**Fig. 2 Surface grid resolution of the TRAM baseline rotor and spinner component grids.**

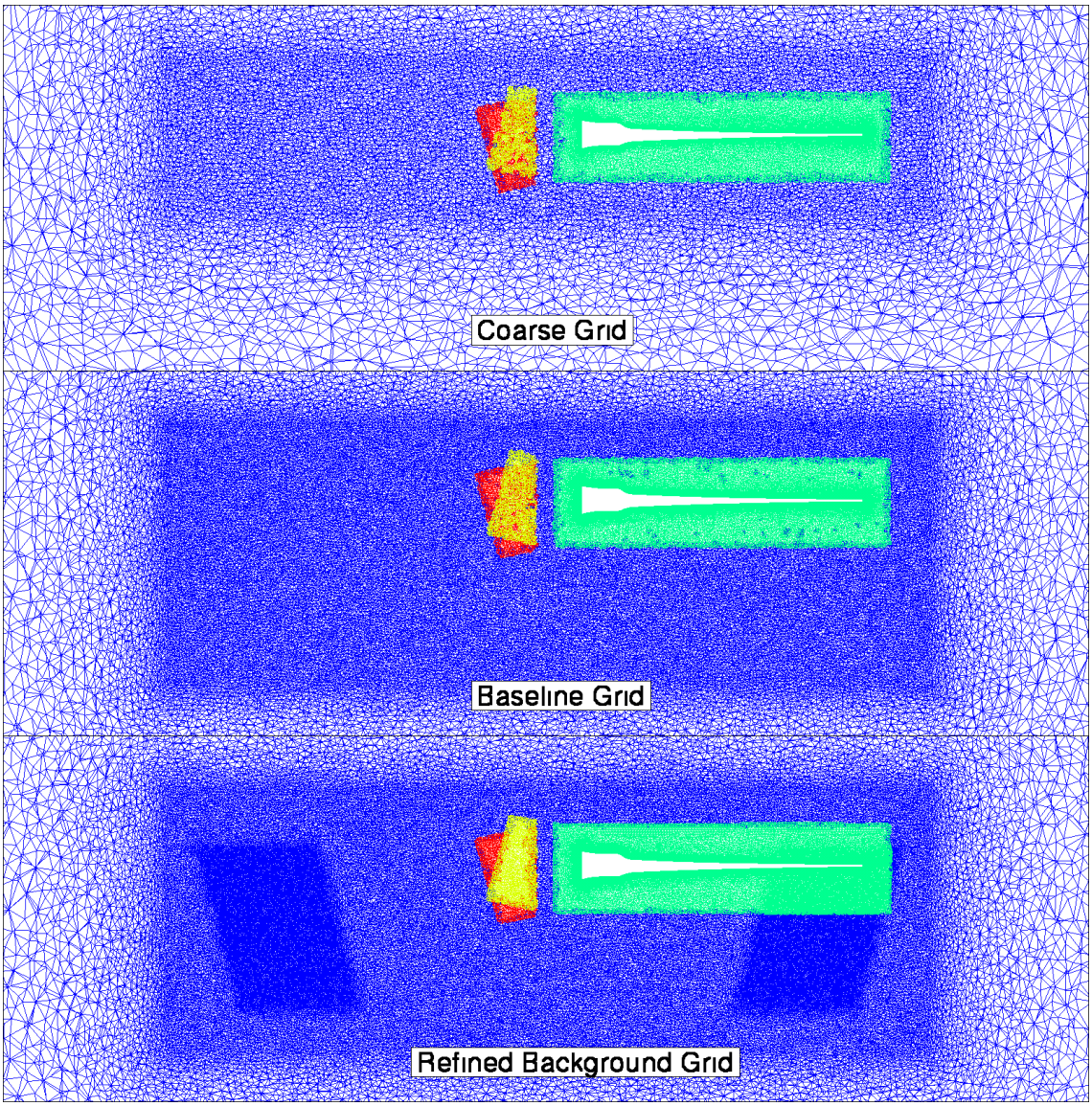


**Fig. 3 Slices through the coasrse, baseline and refined-background TRAM composite grids: green, red, yellow – near-body, blue – off-body.**

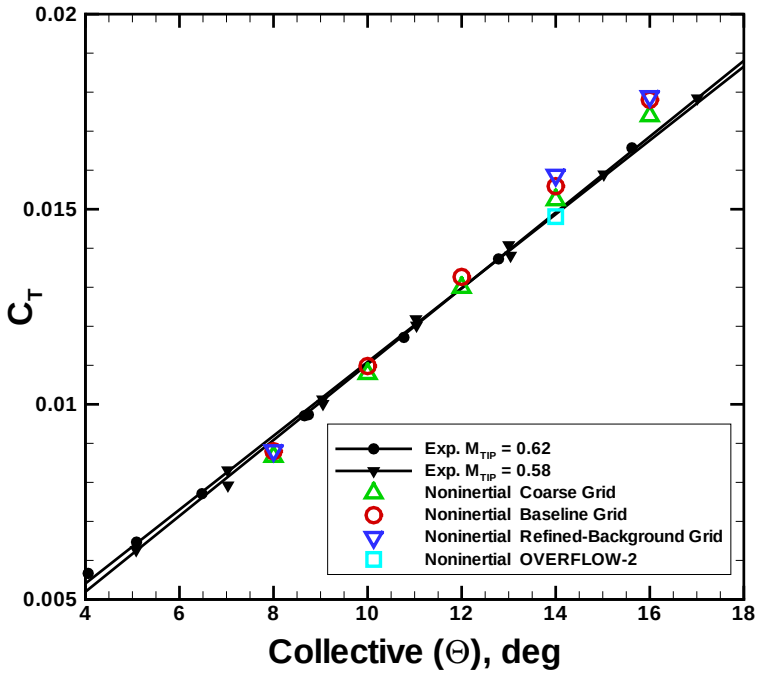


**Fig. 4 Isolated TRAM rotor hover performance in terms of thrust coefficient vs. collective.**

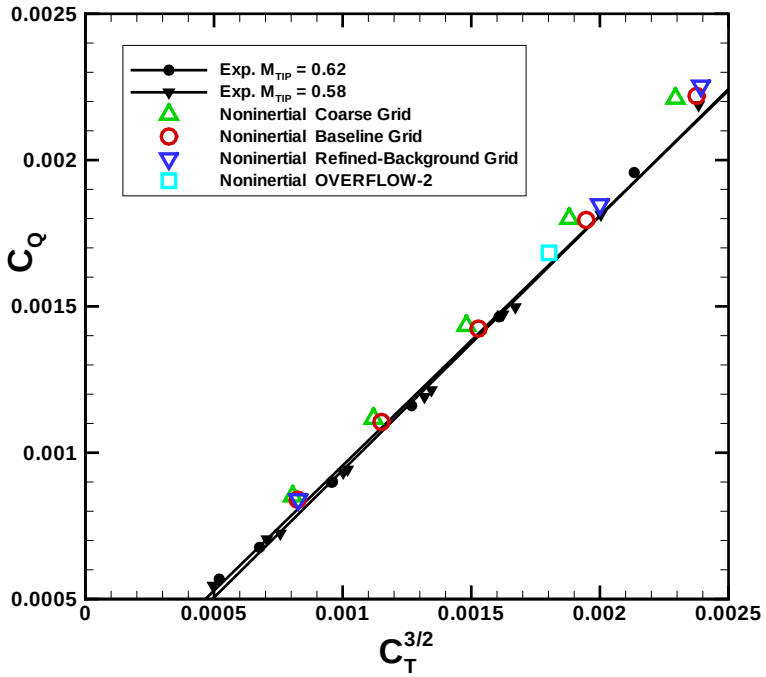


**Fig. 5 Isolated TRAM rotor hover performance in terms of torque coefficient vs. thrust coefficient.**

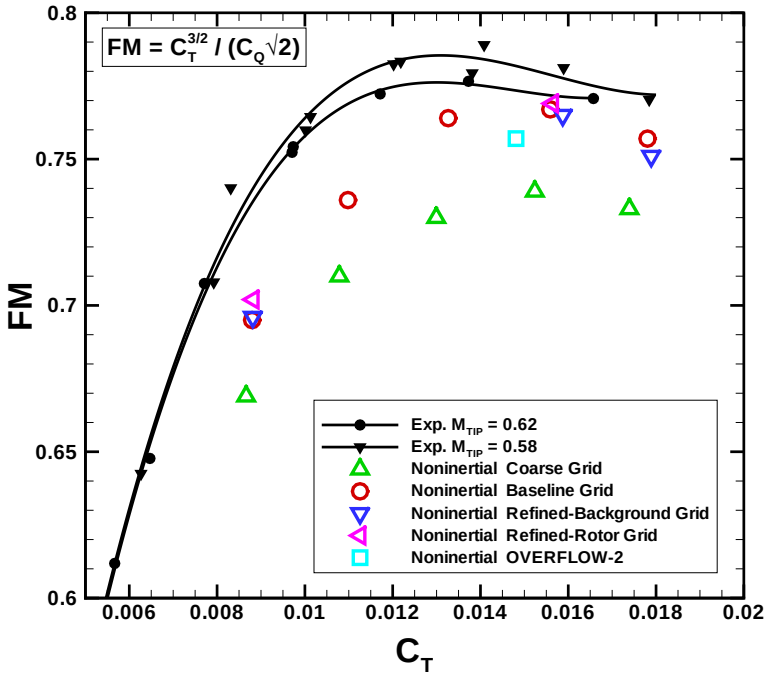


**Fig. 6 Isolated TRAM rotor hover performance in terms of figure of merit vs. thrust coefficient (OVERFLOW-2 results from Ref. 5).**

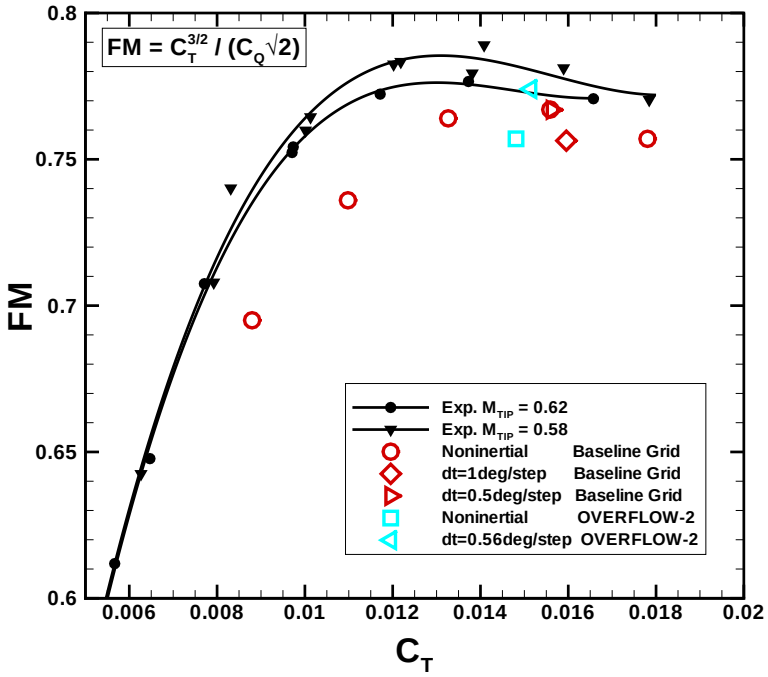


**Fig. 7 Effect of temporal refinement on TRAM rotor hover performance in terms of figure of merit vs. thrust coefficient at 14 deg. collective angle (OVERFLOW-2 results from Ref. 5).**

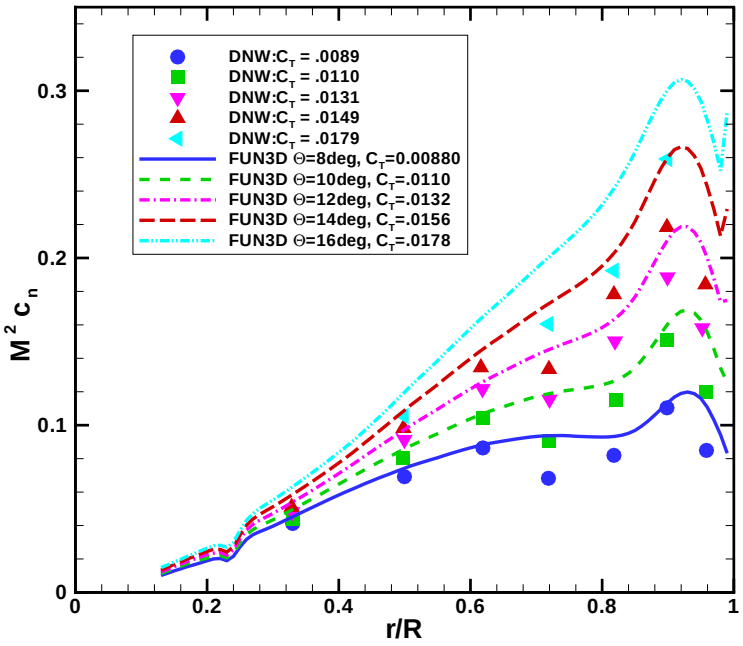


**Fig. 8 Isolated TRAM rotor normal force distributions on the baseline grids.**

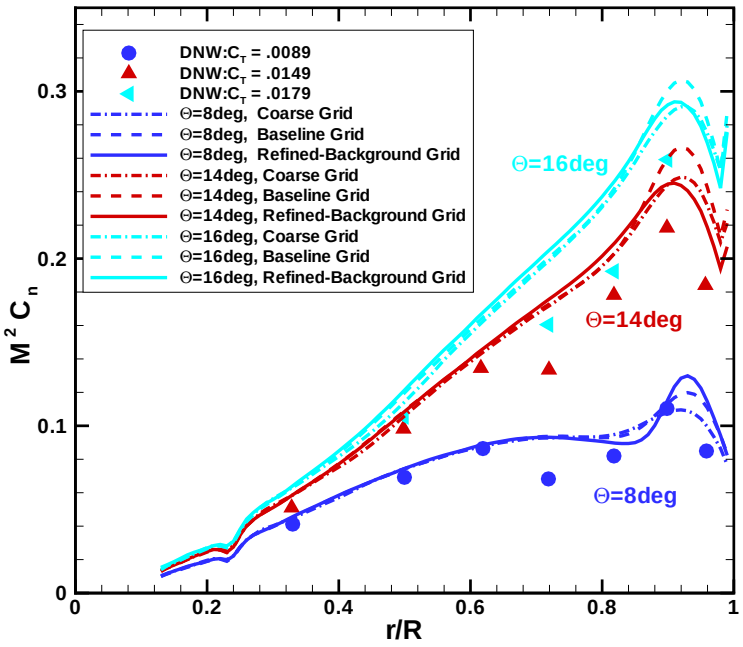


**Fig. 9 Grid convergence of the isolated TRAM rotor normal force distributions.**

(a) Coarse Composite Grid

(b) Baseline Composite Grid

(c) Refined-Background Composite Grid

(d) Refined-Rotor Composite Grid

**Fig. 10 Effect of grid refinement on isolated TRAM rotor surface restricted streamlines in the blade reference frame at 14 deg. collective angle**

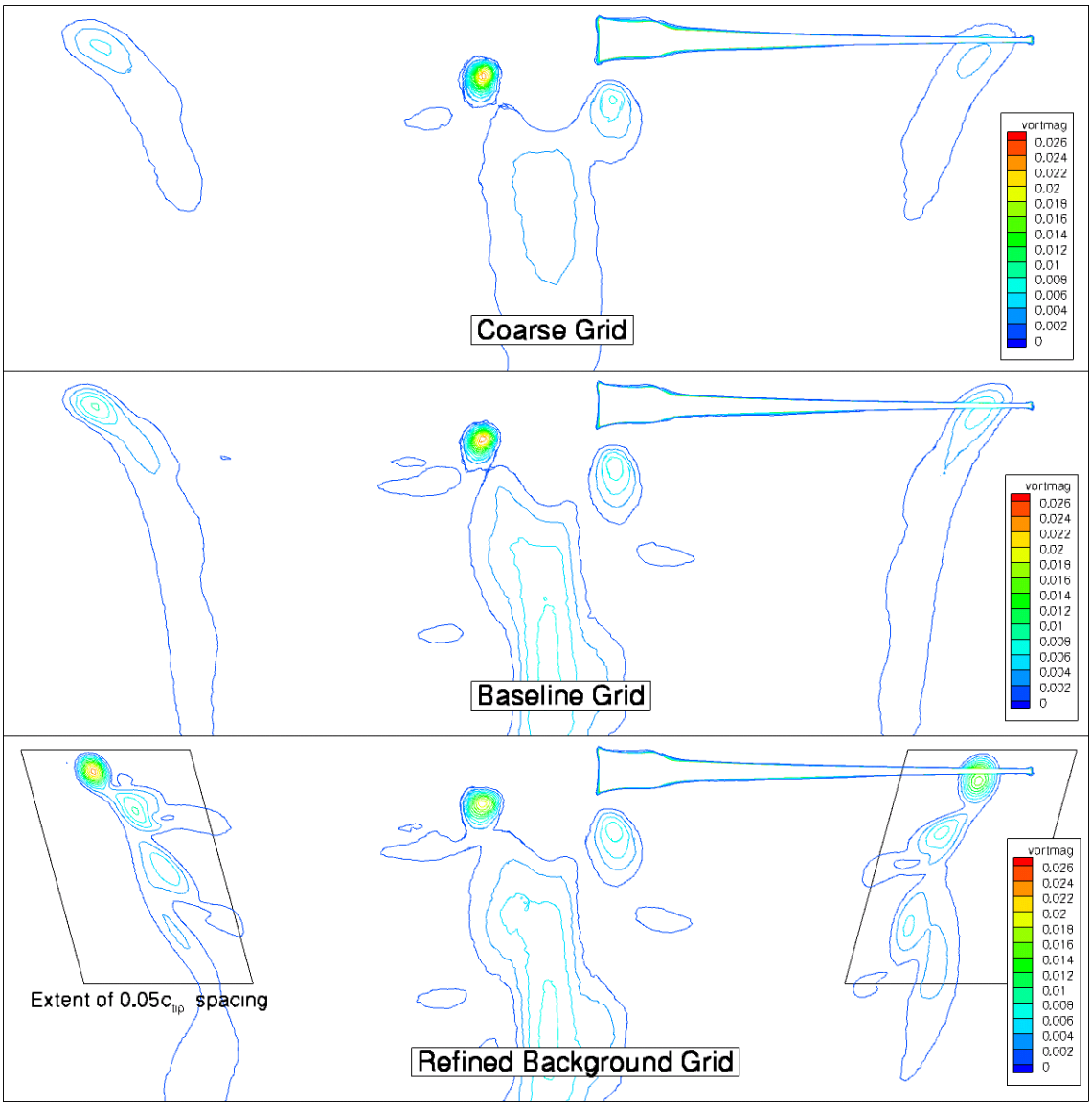


**Fig. 11 Isolated TRAM rotor vorticity magnitude contours at 8 deg. collective angle.**

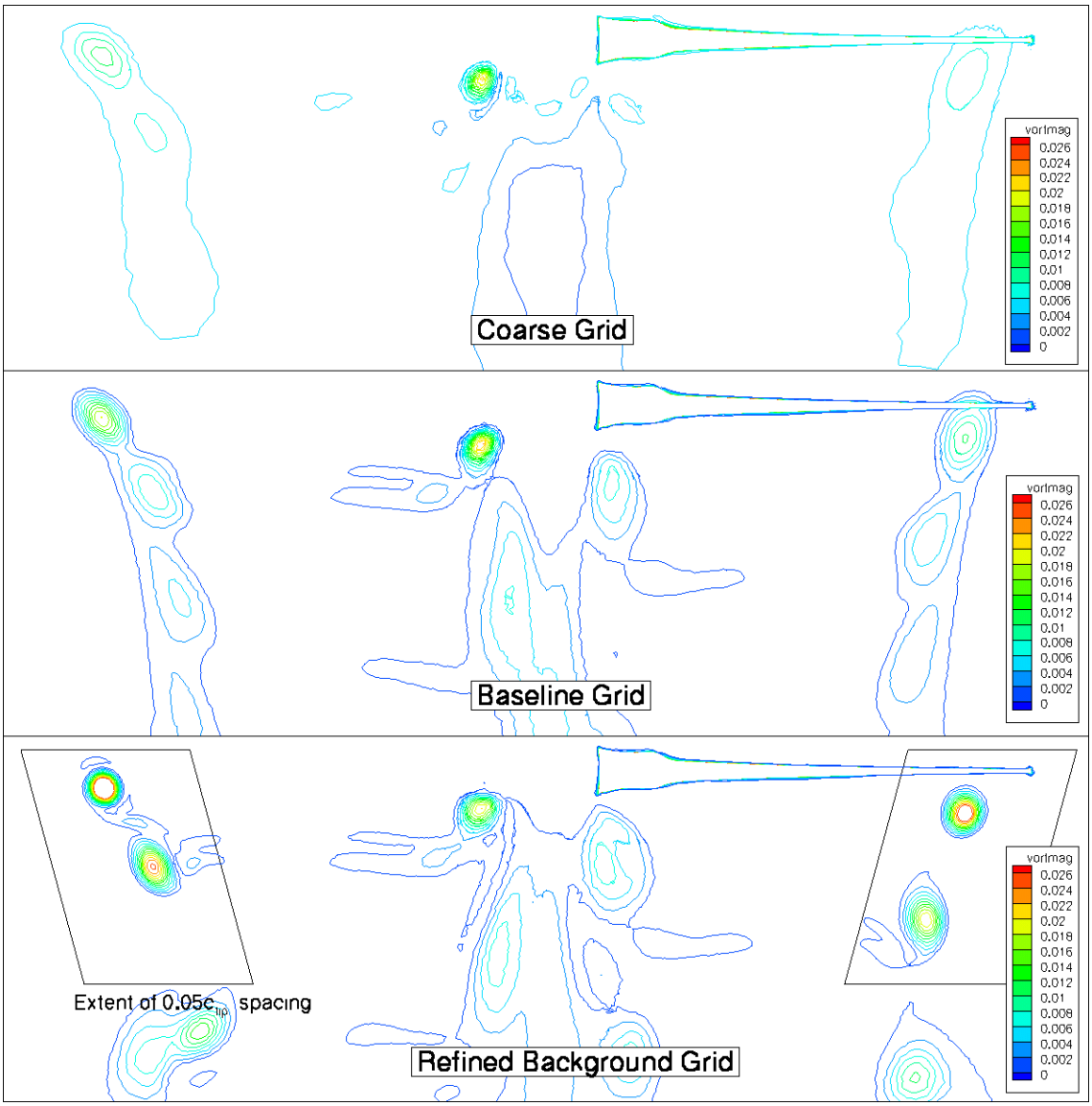


**Fig. 12 Isolated TRAM rotor vorticity magnitude contours at 14 deg. collective angle.**

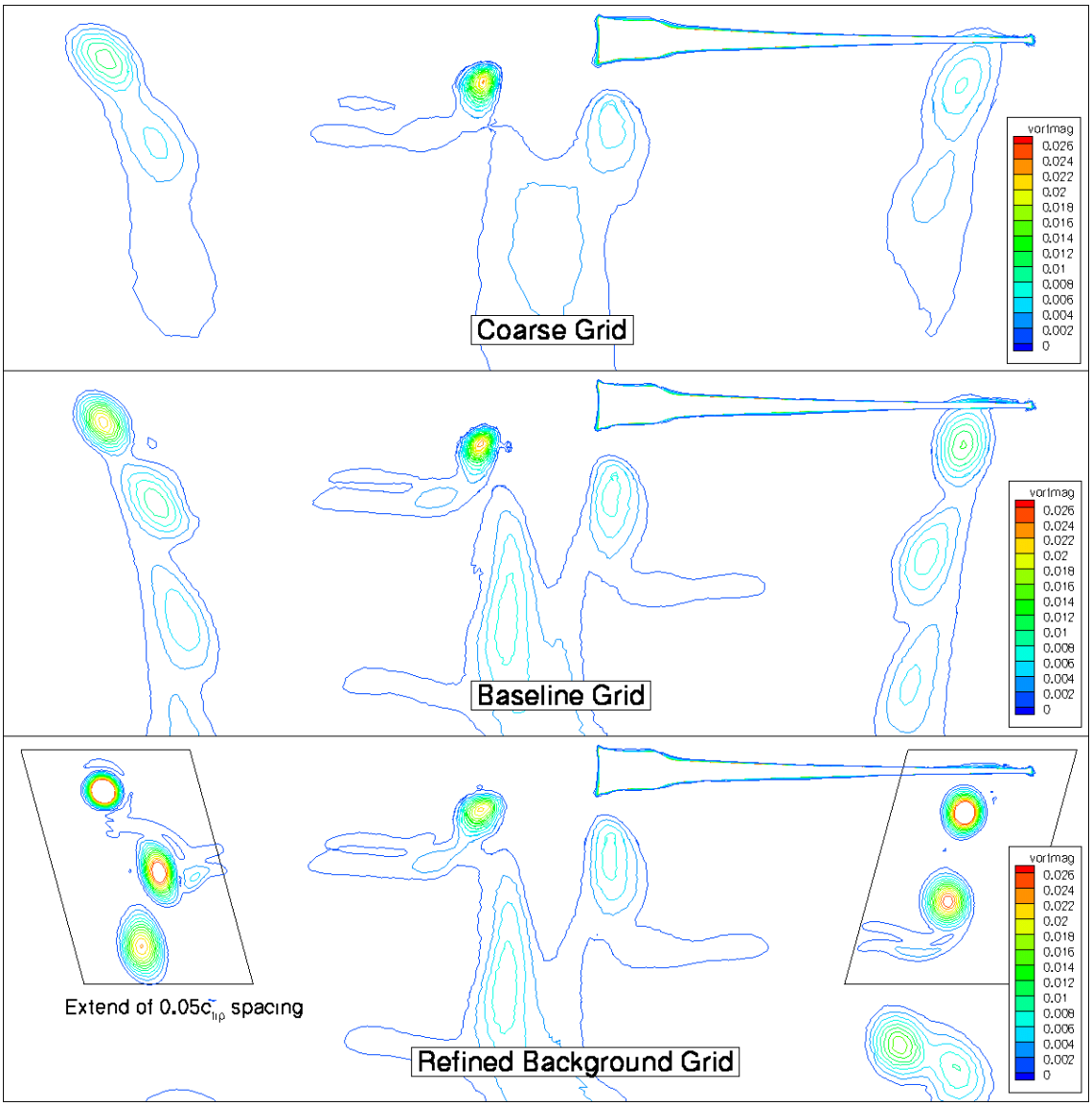


**Fig. 13 Isolated TRAM rotor vorticity magnitude contours at 16 deg. collective angle.**

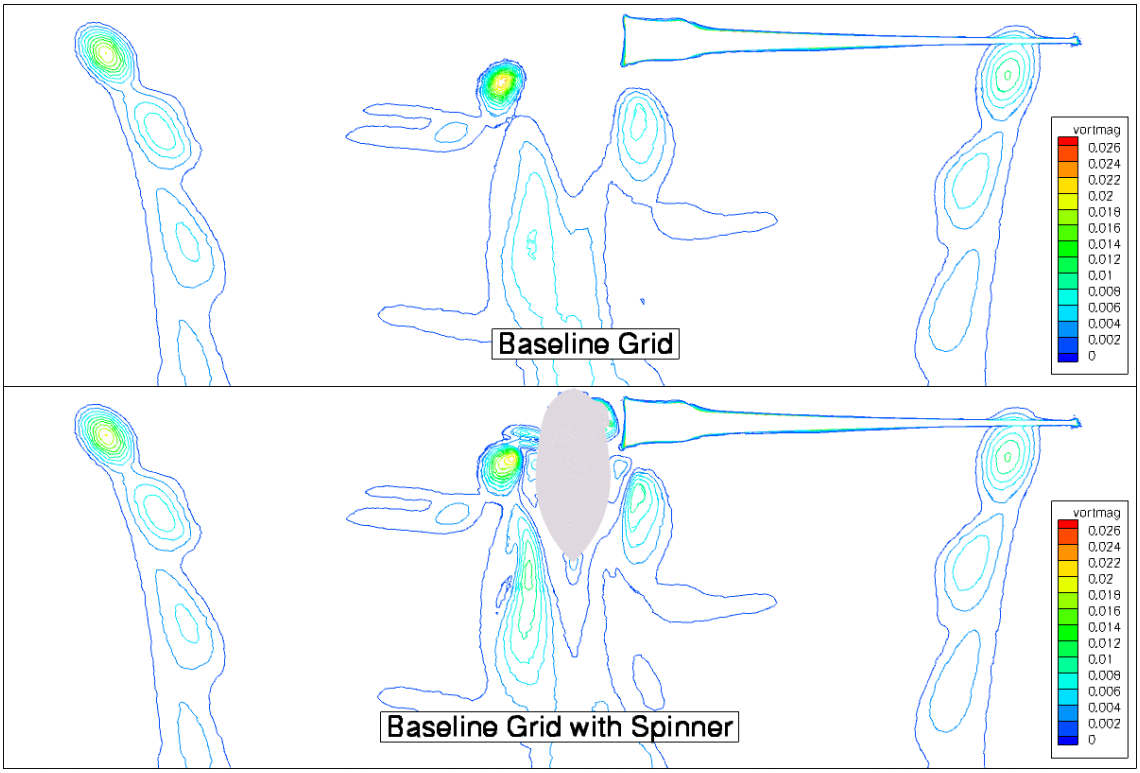


**Fig. 14 Effect of spinner on TRAM rotor vorticity magnitude contours at 14 deg. collective angle.**